Coiled Phononic Crystal with Periodic Rotational Locking: Subwavelength Bragg Band Gaps

Carson L. Willey, Vincent W. Chen, David Roca, Armin Kianfar, Mahmoud I. Hussein, and Abigail T. Juhl

Phys. Rev. Applied **18**, 014035 — Published 15 July 2022

DOI: 10.1103/PhysRevApplied.18.014035

Coiled phononic crystal with periodic rotational locking: Subwavelength Bragg band gaps

Carson L. Willey and Vincent W. Chen
Air Force Research Laboratory, Wright-Patterson AFB, Ohio 45433, USA and UES, Inc., Dayton, OH, 45432, USA

David Roca
Centre Internacional de Mètodes Numèrics en Enginyeria (CIMNE), Universitat Politècnica de Catalunya, Barcelona 08034, Spain

Armin Kianfar
Smead Department of Aerospace Engineering Sciences, University of Colorado Boulder, Boulder, Colorado 80303, USA

Mahmoud I. Hussein*
Smead Department of Aerospace Engineering Sciences, University of Colorado Boulder, Boulder, Colorado 80303, USA and Department of Physics, University of Colorado Boulder, Boulder, Colorado 80302, USA

Abigail T. Juhl†
Air Force Research Laboratory, Wright-Patterson AFB, OH, 45433, USA

(Dated: June 21, 2022)

Phononic crystals (PnC) are spatially periodic materials with band gaps that form by Bragg scattering of elastic waves. Within the frequency range of a band gap, wave propagation is not admitted. A long-standing limitation of this class of materials is that the wavelength for band-gap formation must be on the order of the unit-cell size. This restricts the presence of band gaps to relatively high frequencies for a given lattice spacing. Locally resonant metamaterials, on the other hand, enable the opening of low-frequency, subwavelength band gaps through resonance hybridization. However, their band gaps are characteristically narrow and require large or massive local resonators to form. Here, we break both limitations using beam-based PnCs by (1) locking the rotation degree of freedom at the edges of the primitive unit cell, and (2) coiling the PnC by applying full beam-axis rotations at the locked locations. These respective kinematic and geometric transformations convert a conventional beam PnC from its extended form with a nominal lattice constant to an extremely compact coiled configuration with a greatly reduced lattice constant. With the periodic rotational locking, the band gaps remain intact and are still large, and in fact increase noticeably in size. With the subsequent coiling, the band gaps remain based on Bragg scattering and are quantitively conserved except now appearing at lower frequencies as dictated by the ratio of the extended-to-coiled lattice constants. This ratio defines a coiling factor which is a measure of the reduction in the PnC unit-cell length in the direction of wave transmission while maintaining the normalized band structure of its original extended form except for the favorable changes induced by the periodic rotational locking. A coiling factor of β lowers, by construction, the location of the central frequency of any given band gap by a factor of β. The only limitation is the need for lateral space to accommodate the coiling of the beam segments. The vibration behavior of a finite version of the coiled structure is experimentally tested demonstrating a matching band-gap response, despite the reduction in length, to that obtained by finite-element analysis of the extended rotationally locked version. This concept creates effectively subwavelength Bragg band gaps. It clears the path for PnCs to serve in applications that are orders-of-magnitude smaller in scale than are currently possible, while featuring band gaps that are significantly larger than those generated by locally resonant metamaterials.

I. INTRODUCTION

Phononic crystals are artificially constructed spatially periodic materials that resemble atomic crystals in their wave propagation characteristics. [1–3] One-dimensional (1D) PnCs are typically constructed by alternating between segments of two constituent materials or cross-sectional areas that have differing mechanical impedance. [4]. Elastic waves with wavelengths on the order of the PnC periodicity are scattered due to Bragg interferences, while waves at other frequencies are able to propagate through the material [5–8]. The bandwidth of nonpropagating waves within the PnC is de-

* mih@colorado.edu
† abigail.juhl.1@us.af.mil

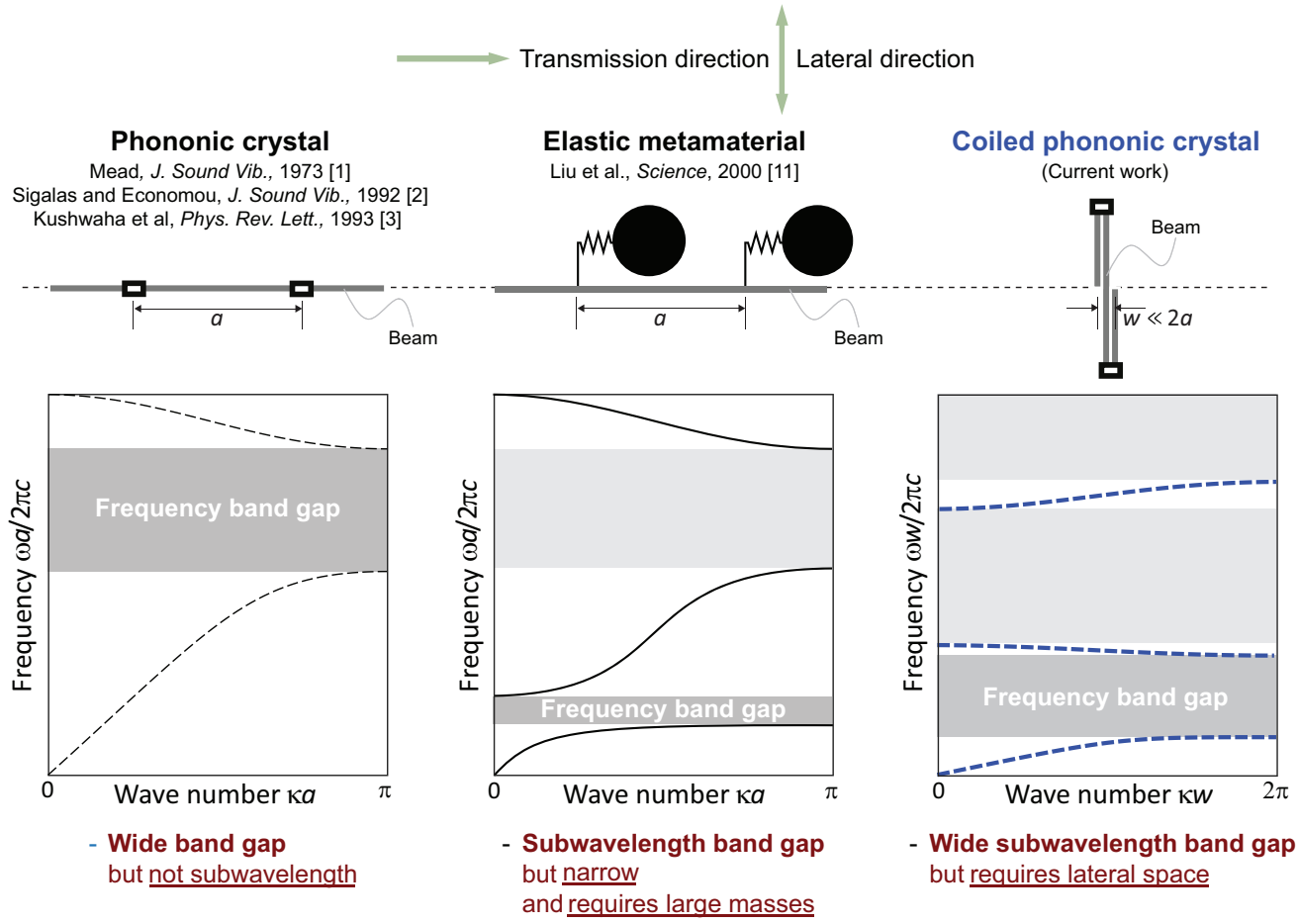

Figure 1. (Color online) Schematic illustration of the two key classes of conventional phononic materials, phononic crystals (left) and elastic metamaterials (middle), and of the proposed coiled phononic crystal concept (right). Top row: spatial configuration of beam-based unit cells. Bottom row: schematics of typical band structure showing basic dispersion/band-gap characteristics. The advantages (in bold) and disadvantages (underlined) of each type of material class are listed.

noted the *phononic band gap*. The frequency-dependence of the propagation properties makes PnCs applicable to noise and vibration mitigation, waveguiding, filtering, etc. [9, 10]. Their ability to act as acoustic/elastic wave filters depends on the geometric structure and material properties of the constituent configuration at the unit-cell level. When low-frequency acoustic/elastic wave mitigation is desired, a PnC is required to be overly large (i.e., long along the direction of transmission) because the periodicity of the unit cell must be on the order of the large wavelength. In the seminal work of Liu et al, [11], it is demonstrated that the introduction of intrinsic resonators in each unit cell allows for a subwavelength band gap to be generated, bringing rise to the concept of a locally resonant elastic metamaterial (EMM) which enables band gaps at wavelengths much larger than the unit-cell dimensions [5, 8, 12]. Unlike Bragg band gaps, these are based on couplings between local resonances and dispersion curves of the host medium—a mechanism that characteristically produces narrow band gaps, however. Furthermore, for the local resonances to be sufficiently low in frequency, usually large or heavy resonators are needed [13–15], which imposes practical design limitations. Some recent efforts explored geometrically complex unit cells with resonant moieties [16, 17] or unit cells with thin bistable elements [18] in pursuit of low-frequency, lightweight metamaterials. Another approach to placing the band gap at low frequencies without introducing large or massive substructures is to design EMMs comprised of responsive materials, in which the application of an active external force dynamically tunes the location of the band gap to the frequency of interest [19–22]. Another path for the generation of subwavelength band gaps is via inertial amplification [15, 23]. This route utilizes intrinsic lever-arm mechanisms to create band gaps by inertial couplings with the base medium. While it enables larger band gaps than local resonances, the band gaps are still restricted in size compared to Bragg band gaps and require relatively long moment arms to reach low frequencies. Moreover, the amplifier mechanism often comprises overly thin ligaments for practical realization, causing load-bearing design limitations [24].

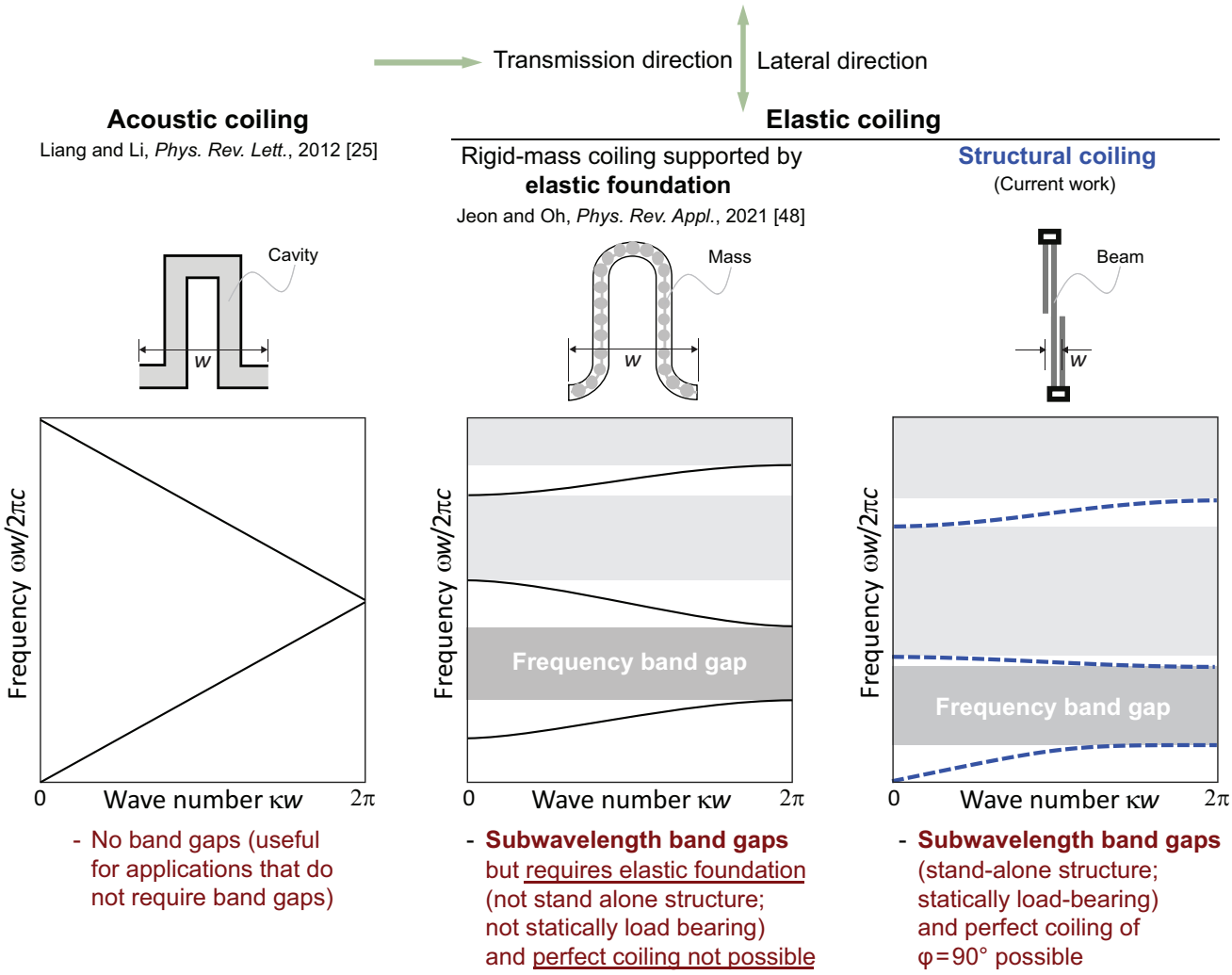

Figure 2. (Color online) Schematic illustration of the concept of coiling as applied to acoustic waves (left) and elastic waves (middle and right). Proposed structural coiling concept (right) is contrasted to rigid-mass coiling with the support of an elastic foundation (middle). Top row: spatial configuration of coiled unit cells. Bottom row: schematics of typical band structure showing basic dispersion/band-gap characteristics. The advantages (in bold) and disadvantages (underlined) of each type of material-coiling are listed.

One approach to achieve space-saving design in resonant metamaterials is to *coil* the material in space [25]. This was shown to enable large refractive index and extreme effective properties. For sound mitigation, acoustic metamaterials (AMM) have been created from ducts with sub-wavelength widths, and lengths that support Fabry-Perot resonances, [26] capable of extraordinary acoustic transmission (EAT). Conventional control of high frequencies allows for the use of a fairly short duct set into a rigid sheet, but when frequencies are low, and acoustic wavelengths are long, a thick sheet is required. To solve this problem, multiple research groups have coiled the length of the cavity, either in a flat coiled duct with perforated face and backing sheets, as in [27], or by coiling the duct in a serpentine pattern along the direction of net wave transmission through the sheet, referred to as labyrinthine AMM, as in [28, 29], or interdigitated channel AMM, as in [25, 30]. While these structures do facilitate EAT, they also come with the drawback of a longer path length of wave propagation leading to higher losses [31, 32]. In spite of these challenges, EAT AMM have been used in applications such as lensing [33], acoustic analog computing [34], a passive multiplexer [35], a component for energy harvesting [36], and for tunable acoustic absorption [37, 38]. Efforts at investigating related structures composed of coiled acoustic cavities created by fractal repetition of rigid walls have been carried out as well [39–42].

While space coiling has been demonstrated to be feasible in acoustics, this is not the case for elastic structures given the tensorial and coupled nature of elastic waves. Lattice materials comprising a periodic pattern of inclined interconnected beam elements [43, 44] achieve some space savings for band-gap performance compared

to a square lattice created from an arrangement of horizontal and vertical beams [45]. Wang et al. considered a 2D beam-based lattice configuration with the beam elements forming a "zig-zag" pattern [46]. It was shown that band gaps form and drop in frequency when the inclination angle in the zig-zag element is increased. However, band-structure conservation is not possible in such systems, and, furthermore, the zig-zag inclination angle is limited by the 2D geometry of the unit cell. Thus perfect and maximum elastic coiling is not possible in conventional lattice materials. Liu et al. examined full (i.e., 90°) elastic coiling but only in the context of a circular device designed to manipulate a point source [47]. The coiled elements in this device were designed to enable control of phase discontinuity and not space savings for band-gap properties.

Despite the limitations associated with elastic coiling, a recent study has examined subwavelength elastic coiling by linking a series of discrete units via "fluidlike connections" realized by springs whereby the entire configuration necessarily follows an "isocurvature path" and must be supported on a elastic foundation such as a rail [48]. While this approach produces a Bragg-type band gap in the subwavelength regime, the system does not yield a stand-alone load-bearing structure that exhibits a static stiffness in the long-wave limit. This is in addtion to the degree of coiling being limited fundamentally by the level of curvature permitted.

In this paper, we present a coiled PnC configuration that exhibits both wide and subwavelength band gaps, and that is a stand-alone load-bearing structure with a well-defined static stiffness in the long-wave limit. Our configuration is based on two key transformations applied to an extended beam structure consisting of repeated segments with a localized mass attached at each junction between the segments. The first transformation is kinematic, whereby we impose rotational locking at the edges of the segments where the masses are located. With rotational locking, only longitudinal and transverse displacements are admitted at these junctions; everywhere else along the beam segments a rotational degree of freedom also exists. We demonstrate that the periodic rotational locking constraint preserves the Bragg band gaps and in fact markedly increases their sizes. The second transformation is purely geometric, whereby each beam segment is fully rotated, by construction, to form a final serpentine configuration with a full $|\phi| = 90°$ angle of rotation enforced along the beam axis for each segment, thus providing extreme coiling as demonstrated in the top-right of Fig. 1. These two transformations combined enable drastic space-saving along the direction of wave transmission while allowing for wide Bragg band gaps to still appear, except now with the profound advantage of lying deep in the subwavelength regime. This is in contrast to the wide but necessarily superwavelength band gaps permitted by the conventional extended form of the beam PnC and to the subwavelength but narrow band gaps enabled by attaching local resonators to the PnC. Figure 1 provides a schematic illustrating the contrast between the three concepts−the two classical types of phononic materials and the proposed coiled type−with a summary of the pros and cons. The same fundamental limitations apply to other configurations (1D, 2D, and 3D) of conventional PnCs and locally resonant elastic metamaterials [10]. Figure 2, on the other hand, contrasts the proposed concept to the notions of acoustic coiling and elastic coiling with the support of an elastic foundation, and again listing the advantages/disadvantages of each−noting that acoustic coiling has not been shown to produce subwavelength band gaps.

To visually demonstrate the practical utility of the proposed concept, we show in Fig. 3 an example in which two competing sets of PnC structures support a common piece of domestic rotating machinery (e.g., a standard washing machine) to prevent the transmission of vibrations to the floor. In the first case, shown in Fig. 3(a), a conventional PnC−in its usual extended form−is used. The PnC comprises elastic beam segments with rigid masses at the junctions between the segments to induce periodicity. Due to the low operating frequency (less than 50 Hz), this structure is too long for practical consideration. In contrast, in the second case, shown in Fig. 3(b), the proposed corresponding coiled PnC is utilized. This structure is extremely short, thus suitable for practical deployment, yet also exhibits both large and low-frequency band gaps as needed by the application. The space savings along the vertical direction enabled by this outcome is indicated by the dashed black box. The only drawback is the need for lateral space to accommodate the coiling, which in this case, as in many applications, is available. In addition to conventional vibration isolation applications, contemporary phononics-based technologies would also benefit immensely from space savings, such as phononic subsurfaces (PSubs) used for passive flow control [49]. Perfect elastic coiling would also advance the engineering of elastic metasurfaces with desired refractive properties through advanced control of phase shifting [47]−in analogy to current applications of acoustic coiling [25].

II. FINITE-ELEMENT MODELING OF COILED PHONONIC CRYSTAL

We consider a general coiled beam PnC configuration as shown by the schematics provided at the top of Fig. 4. Given its periodicity, only a single unit cell is examined for dispersion analysis. The unit cell consists of a central beam segment and a half-beam segment at each side. A rigid mass is attached at each junction connecting the segments; the addition of this mass will be shown to be valuable for experimental realization of the model. The angle ϕ, referred to earlier, is defined as shown in Fig. 4, to represent the angular orientation of the beam segments. In one extreme, at $\phi = 0°$, we ob-

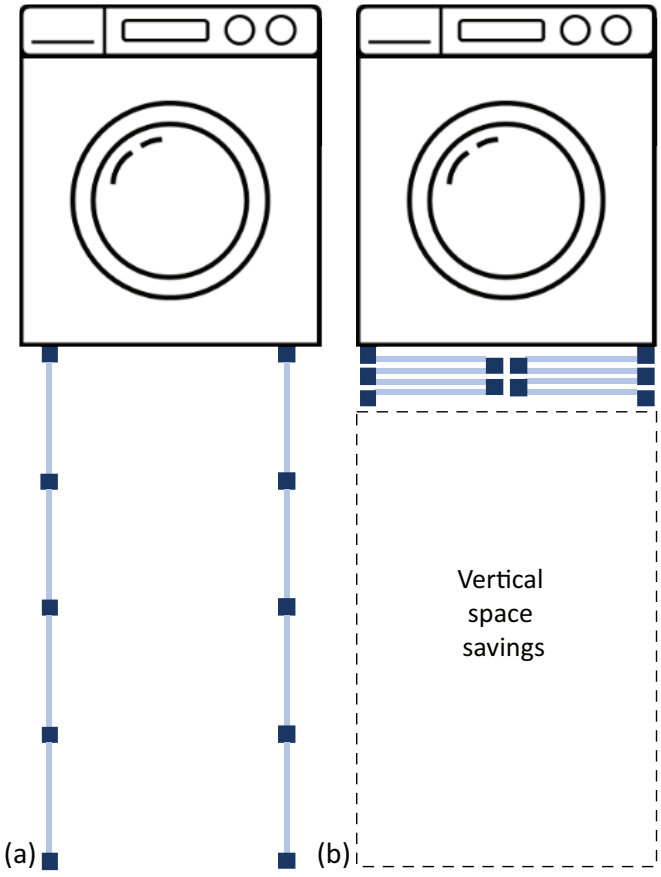

Figure 3. (Color online) Application of coiled PnC concept to rotating machinery such as a washing machine. To reduce the transmission of vibrations to the ground, the machine can be isolated by (a) a conventional beam-mass-based PnC where the unit cells are necessarily long to target the frequency of interest (impractical), or by (b) the proposed coiled beam-mass-based PnC which may be orders of magnitude shorter in the direction of transmission (practical). The region of space-saving along the vertical direction is highlighted.

tain a beam PnC in its conventional extended form as shown in the top-left of Fig. 4. At the other extreme, at $\phi = 90°$, a fully coiled PnC configuration emerges as shown on the top-right of Fig. 4. At intermediate angles, a lattice structure with inclined beam segments is generated as the one depicted at the top-center.

We model the beam segments using a combination of rod theory and Euler-Bernoulli theory [50] such that each material point along the beam's neutral axis admits three local displacements: longitudinal $u(x,t)$, transverse $v(x,t)$, and rotational $\theta(x,t) = dv/dx$. The longitudinal motion is governed by the rod equation

$$c_r^2 u'' - \ddot{u} = 0, \tag{1}$$

and the transverse and rotational motions by the Euler-Bernoulli beam equation

$$c^2 v'''' + \ddot{v} = 0, \tag{2}$$

with constants $c_r = \sqrt{E/\rho}$ and $c = \sqrt{EI/\rho A}$, where E, ρ, A, and I denote the Young's modulus, density, area, and moment of inertia of the cross-section, respectively. The primes refer to a derivative with respect to the neutral axis coordinate, while the overdots refer to differentiation with respect to time.

We use the finite-element (FE) method [51] to discretize the beam segments, yielding what is commonly referred to as frame elements in which both axial and flexural motions are incorporated [52]. The stiffness and mass matrices for frame elements are given in Appendix A, and the mass matrix for the rigid mass placed at the junction between each beam segment is given in Appendix B.

The above elemental formulation is used to formulate the assembled global set of equations of motion for the unit cell, which takes the form $\mathbf{M}\ddot{\mathbf{q}} + \mathbf{K}\mathbf{q} = \mathbf{0}$, where the matrices $\mathbf{M}$ and $\mathbf{K}$ denote the global mass and stiffness matrices, respectively. The vectors $\mathbf{q}$ and $\ddot{\mathbf{q}}$, respectively, denote the nodal displacements and their corresponding accelerations. For any jth node, the nodal displacement vector in global coordinates is given by $\mathbf{q}_j = (u_j, v_j, \theta_j)^{\mathrm{T}}$.

Assuming harmonic motion in time,

$$\mathbf{q} = \mathbf{U}e^{\mathrm{i}\omega t}, \tag{3}$$

where ω and t denote frequency and time, respectively, and $\mathrm{i} = \sqrt{-1}$ is the imaginary unit, the matrix equation becomes

$$(\mathbf{K} - \omega^2\mathbf{M})\mathbf{U} = \mathbf{D}\mathbf{U} = \mathbf{0}, \tag{4}$$

where $\mathbf{D}$ is the dynamic stiffness matrix. Dispersion curves and associated mode shapes may then be readily computed. Given that our model is comprised of serially connected units admitting 1D wave propagation, the displacement of the first and last nodes in the unit cell are related by the phase shift imposed by the wavenumber κ of a traveling Bloch wave [53]. Specifically, we write

$$\mathbf{U} = \begin{bmatrix} \mathbf{I} & \dots & \mathbf{0} \\ \vdots & \ddots & \vdots \\ \mathbf{0} & \dots & \mathbf{I} \\ e^{\mathrm{i}\kappa x}\mathbf{I} & \dots & \mathbf{0} \end{bmatrix} \mathbf{U}_B = \mathbf{T}\mathbf{U}_B, \tag{5}$$

where $\mathbf{U}_B$ is the Bloch-wave displacement vector and $\mathbf{I}$ is the identity matrix. Substituting the Bloch-wave matrix relationship into Eq. 4, the Bloch-wave reduced eigenvalue problem is obtained as

$$\mathbf{T}^*\mathbf{D}\mathbf{T}\mathbf{U}_B = \mathbf{D}_B\mathbf{U}_B = \mathbf{0}, \tag{6}$$

where $\mathbf{D}_B$ is the Bloch wave reduced dynamic stiffness matrix and the "$*$" superscript is the complex conjugate (Hermitian) transpose. Equation 6 is solved for a range of wavenumbers κ sweeping the irreducible Brillouin zone to obtain the dispersion curves. The reader is referred to Refs. [54] and [44] for a detailed description of FE modeling of beam-based lattices and calculation of their dispersion curves by Bloch's theorem.

III. BAND-STRUCTURE TRANSFORMATION DUE TO ROTATIONAL LOCKING AND COILING

We now use FE analysis to examine the effects of both the periodic rotational locking and the coiling of the beam segments on the dispersion behavior, and to quantify the implications on space saving. In all studies, 20 finite elements per beam segment were shown to provide sufficiently converged numerical results.

A. Simple canonical model of coiled PnC: Dispersion and coiling factor

A canonical model is considered to investigate the transition from the extended form of our PnC to the fully coiled form by varying the beam segment rotation angle ϕ by increments of 15°. Using the 2D frame-based FE analysis framework described in Section II, we examine cases where the rotation at the beam-segment edges (where the rigid masses are located) is locked versus unlocked. The material and geometric parameters of the model are listed in Table I. The results are shown in Fig. 4 where the dispersion curves are plotted as a function of the wavenumber normalized with respect to the actual unit cell size w, which gets smaller with increasing ϕ. A clear contrast is displayed between the unlocked (thin black dashed) and locked (thick blue dashed) cases.

The band structure for the extended PnC ($\phi = 0°$) clearly has two subsets of independent dispersion curves, where one corresponds to longitudinal wave motion (axial rod behavior), and the second corresponds to bending wave motion (flexural beam behavior). The computational unit cell considered at this angle comprises two primitive unit cells, thus band folding occurs. Once ϕ is changed from zero, the structure contained within the unit cell becomes unique and representative of the primitive configuration.

Without locking, the dispersion curves undergo a "monotonic" transition with ϕ. In contrast, with locking, the curves transform until the midway angle of $\phi = 45°$ and then display a symmetric reversal in their transformation with further increase in ϕ, until the band-structure is fully recovered with full coiling at $\phi = 90°$. At intermediate angles, the longitudinal and transverse displacements are coupled, providing 2D deformation mechanisms. At the extreme coiling case of $\phi = 90°$, without locking, the local axial and bending motions in the beam segments are still uncoupled, but the full coiling alters the transmission kinematics for the transverse motion. However, with the introduction of the periodic locking, the decoupled motions are kinematically unaltered leading to complete conservation of the flexural character of the displacement fields when compared to the nominal extended case of $\phi = 0°$. This behavior represents the key finding that enables the proposed concept of an elastically coiled PnC. In summary, a fully coiled beam-based PnC with rotational locking exhibits an identical band structure (when normalized with respect to the actual unit cell size w) to that of the extended version of the periodically locked PnC−leading to the remarkable advantages highlighted in Fig. 1 with the only limitation that the coiling requires space availability in the lateral direction. In the remainder of this work, we will only consider the extended and fully coiled configurations, where it follows−given the uncoupling and kinematic preservation phenomena described above−that standard 1D beam FE modeling produces identical dispersion curves to that obtained by the 2D FE frame-based model for the $\phi = 90°$ configuration when periodic rotational locking is enforced.

Parameter	Value	Unit
Beam thickness, t	10	mm
Beam width, b	1	mm
Beam-segment length, L	120	mm
Mass edge length, $h = d$	20	mm
Primitive-cell length for $\phi = 0$, $a = L$	120	mm
Primitive-cell length for $\phi = 90°$, $w_{90} = 4s$	20	mm
Offset, $s = d/4$	5	mm
Coiling factor, $\beta = a/w_{90}$	6	
Young's modulus, E	68.9	GPa
Density, ρ	2700	kg/m^3
Periodic mass, m	1	g
Loss factor, η	0	

Table I. Properties of canonical PnC studied in Fig. 4, Fig. 5, and Fig. 6.

Figure 5 presents four sets of dispersion curves for the extended-unlocked (thin black dashed) and extended-locked (thick red), shown in (a), and coiled-unlocked (thin black dashed) and coiled-locked (thick blue dashed), shown in (b). Associated band gaps are marked by transparent pink and blue backgrounds corresponding to the extended-locked and coiled-locked PnC, respectively. The extended-unlocked and coiled-unlocked band gaps are both shaded in gray, Note that in Fig. 5(a), the extended-unlocked band gap is always encompassed within the extended-locked band gap, and thus it appears as a darker pink due to being shown through the transparency. In each case, the lower band-gap edge frequency is identical between the extended-unlocked and extended-locked PnCs, but the rotational locking at the edges of the beam segments has a favorable effect on the upper band-gap edge frequency, driving it up noticeably from that of the extended-unlocked PnC.

As observed in Fig. 4, both extended-locked and coiled-locked PnC dispersion curves are exactly the same when the abscissa is normalized with respect to w and the ordinate is fixed (or normalized with respect to the extended version unit cell length a). However, when the same curves are plotted with respect to a frequency that is also normalized with respect to w, as shown in Fig. 5 (b), the dispersion curves of the coiled-locked case look substantially different due to the reduced lattice spacing.

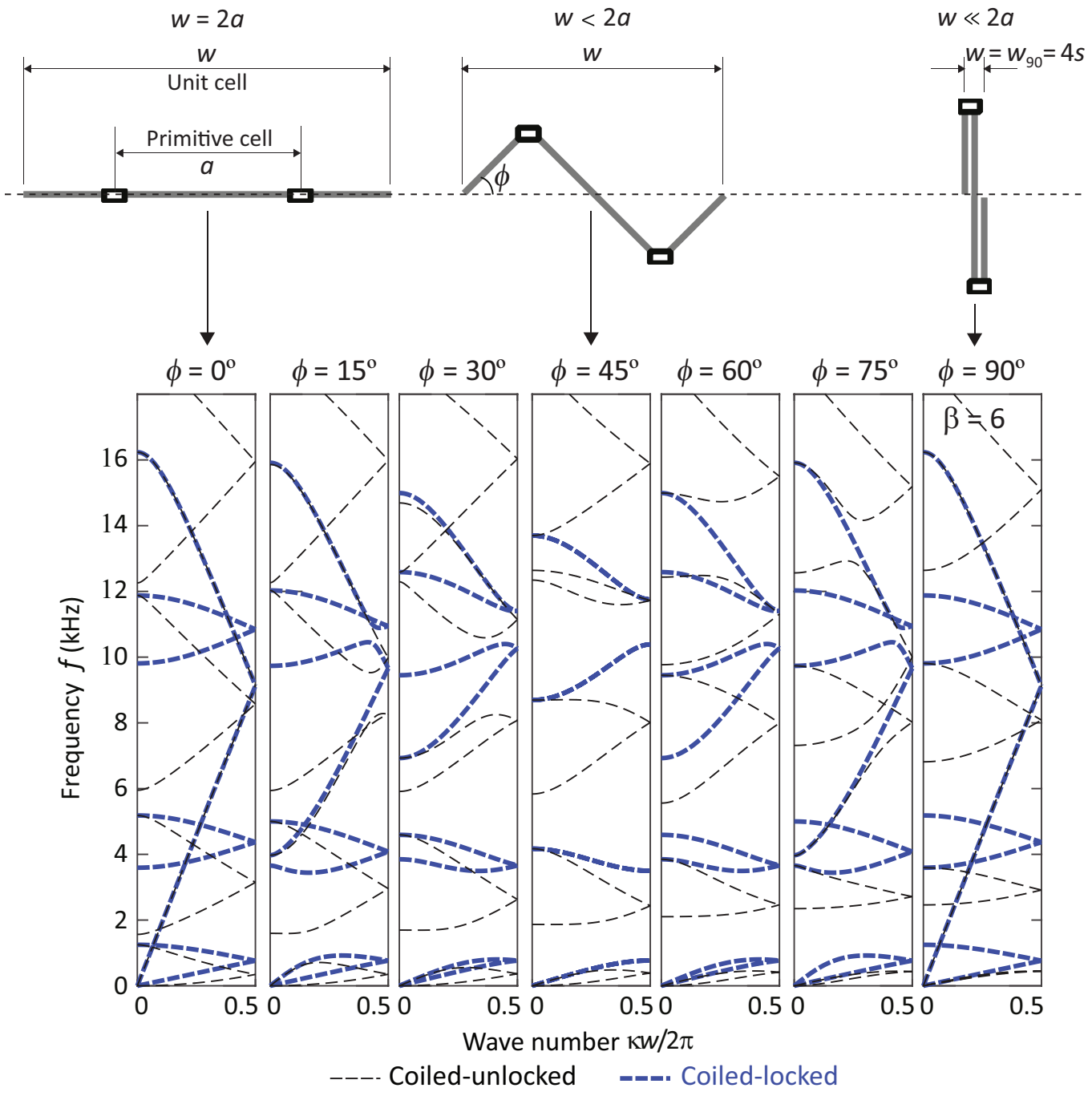

Figure 4. (Color online) Elastic band-structure evolution with beam-segment rotation angle ϕ. Top: Schematics of three unit-cell configurations, corresponding to extended (left), partially coiled (middle), and fully coiled (right) PnC are shown. Bottom: Dispersion curves corresponding to different angles without periodic locking (thin black dashed) and with periodic locking (thick blue dashed). As we progress from left to right, the coiling reduces the unit-cell length w in the direction of the Bloch wave propagation; the horizontal axis is normalized with respect to this varying value of w. For consistent comparison, the unit cell used in the calculations is chosen to be w, which is the smallest possible cell for all angles except for $\phi = 0°$. At $\phi = 0°$, the unit cell is twice as long as the primitive cell ($w = 2a$) as shown. At $\phi = 90°$, the PnC is fully coiled with a coiling factor of $\beta = 6$. Upon comparing the band structure of the coiled-locked PnC at $\phi = 0°$ and $\phi = 90°$, band-structure conservation is demonstrated.

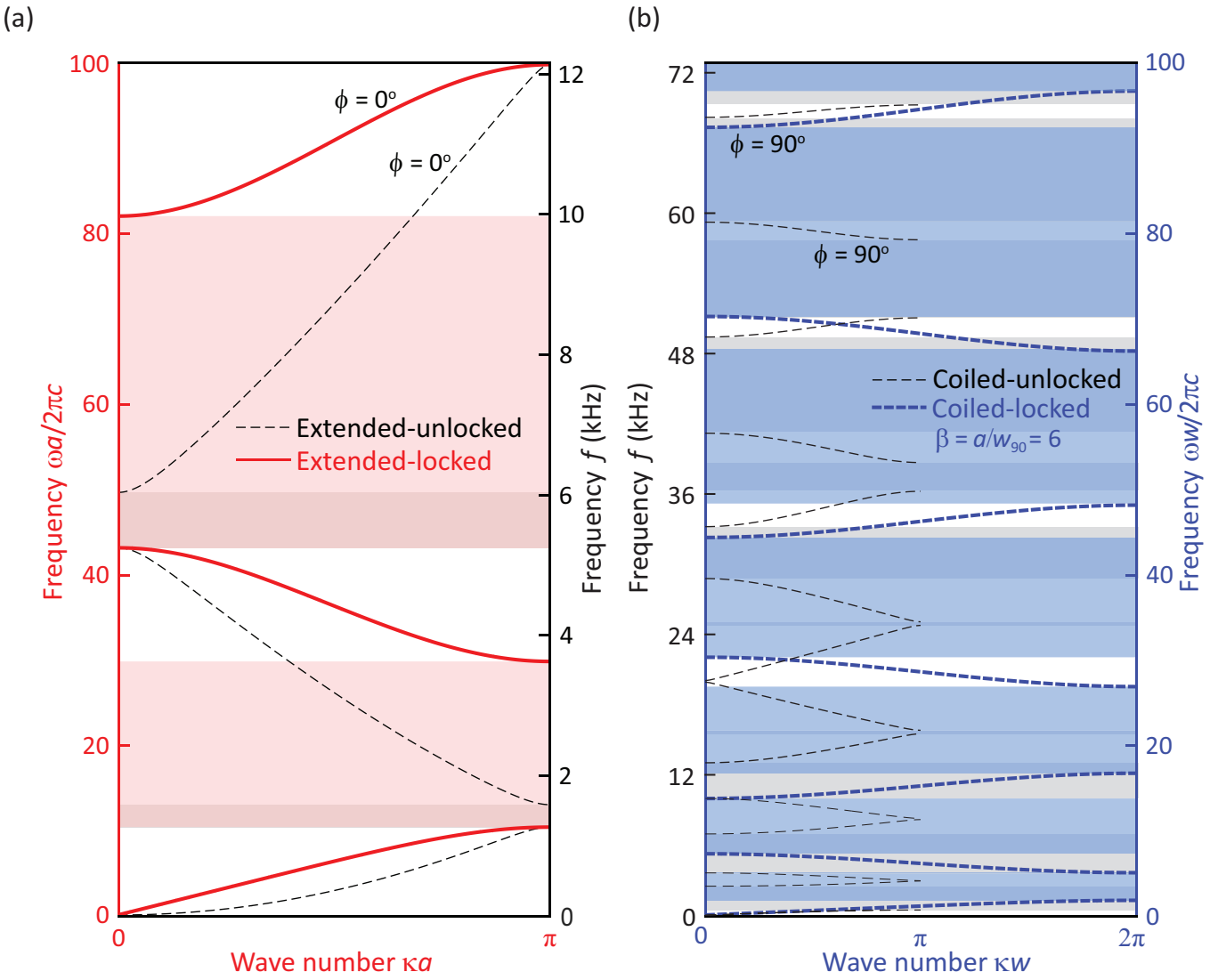

Figure 5. (Color online) Impact of periodic rotational locking and full coiling on the elastic band structure. Dispersion curves for the (a) extended-unlocked (thin black dashed), extended-locked (thick red), (b) coiled-unlocked (thin black dashed), and coiled-locked (thick blue dashed) PnCs are shown where colored vertical axes are given in terms of non-dimensional frequency scaled by $a/(2\pi c)$ in (a) and non-dimensional frequency scaled by $w/(2\pi c)$ in (b). Vertical axes showing the frequency in unite of kHz are also provided. The curves in (a) are for $\phi = 0°$ and in (b) for $\phi = 90°$. In (b), the coiled-unlocked curves are obtained by solving the 2D FE model (as done in Fig. 4), and the coiled-locked curves are identical to the extended-locked curves in (a) except now normalized with respect to the fully coiled unit-cell length.

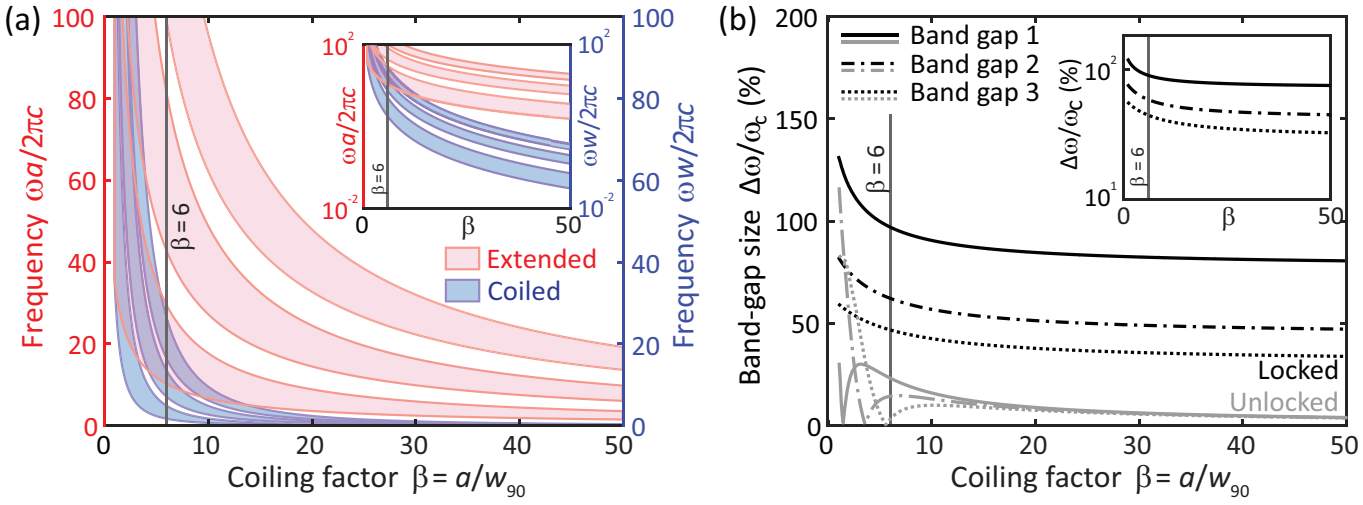

Figure 6. (Color online) Impact of coiling factor on space saving. (a) First three band gaps for the extended-locked PnC (transparent pink) with frequency scaling $a/2\pi c$ (red axis), and the coiled-locked PnC (blue) with frequency scaling $w/2\pi c$ (blue axis) are plotted as functions of the coiling factor β. (b) Normalized bandwidth of the first three band gaps (1st: solid, 2nd: dot-dashed, and 3rd: dotted) are plotted for the locked (black) and unlocked (grey) PnC configurations versus β; this relative quantity is independent of the lattice constant. In (b), the non-monotonic behavior at low values of β for the unlocked case is due to varying the beam segment length while keeping the masses constant. The vertical lines mark the $\beta = 6$ value considered in Fig. 4 and Fig. 5.

The scaling of the dispersion curves frequencies with respect to the reduced lattice constant w versus the extended lattice constant a allows us to directly observe the achievements gained by coiling. On the red vertical axis, the extended PnC has band gaps at frequencies limited by the Bragg condition. By coiling, the same PnC produces band gaps at lower frequencies. The extent of this reduction is directly characterized by a *coiling factor*, defined as

$$\beta = a/w_{90}, \tag{7}$$

which opens the opportunity for the realization of a Bragg band gap for unit cells with subwavelength dimensions along the direction of transmission, as demonstrated in Fig. 5. The $\phi = 90°$ case shown in Fig. 4 and Fig. 5 is for $\beta = 6$.

The relative intervals of the first three band gap versus the coiling factor for the extended-locked (transparent pink) and the coiled-locked (blue) PnCs are shown in Fig. 6(a). The drops in the band-gap locations are shown to be most severe at lower values of β and then nearly saturate at higher values. The normalized bandwidth of each band gap is defined as

$$\Delta\omega/\omega_c = 2(\omega_u - \omega_l)/(\omega_u + \omega_l), \tag{8}$$

where ω_u and ω_l are the upper and lower edge frequencies of each band gap calculated for a given coiling factor.

The relative bandwidth of the same band gaps, the first (solid), second (dot-dashed), and third (dotted), are plotted in Fig. 6(b). One set of curves is shown for the locked cases since the normalized band-gap bandwidths are the same for both the extended-locked and coiled-locked PnC band gaps. The second set of curves correspond to the extended-unlocked case. In this model, the extended primitive cell length a is taken to be equal to the beam-segment length L, while the coiled unit cell length w is $4s$ where s is the offset of the attachment point of the beam-segment end to the rigid mass. Since the rigid mass size is kept constant, the increase in β is achieved by increasing only the length of the beam segments. As the coiling factor increases, the normalized band-gap bandwidths drop; this reduction stems from changes in the Bragg interferences as the segments grow in length, which is independent of the coiling. However, these drops in the relative band-gap size eventually nearly level off with increase in β, and, importantly, their values are still substantially higher for the locked configuration compared to the unlocked configuration. For the locked PnC, the normalized bandwidth of the first band gap is approximately 80% or greater for $\beta \leq 50$, and the third band gap is approximately 35% or greater in the same β range.

B. Practical model of coiled PnC: Dispersion and mode shapes

The second study investigates a model of a more practical configuration for both experimental characterization and industrial deployment. Here we investigate only extended and fully coiled PnC configurations and use only flexural beam elements as done in standard 1D FE anal-

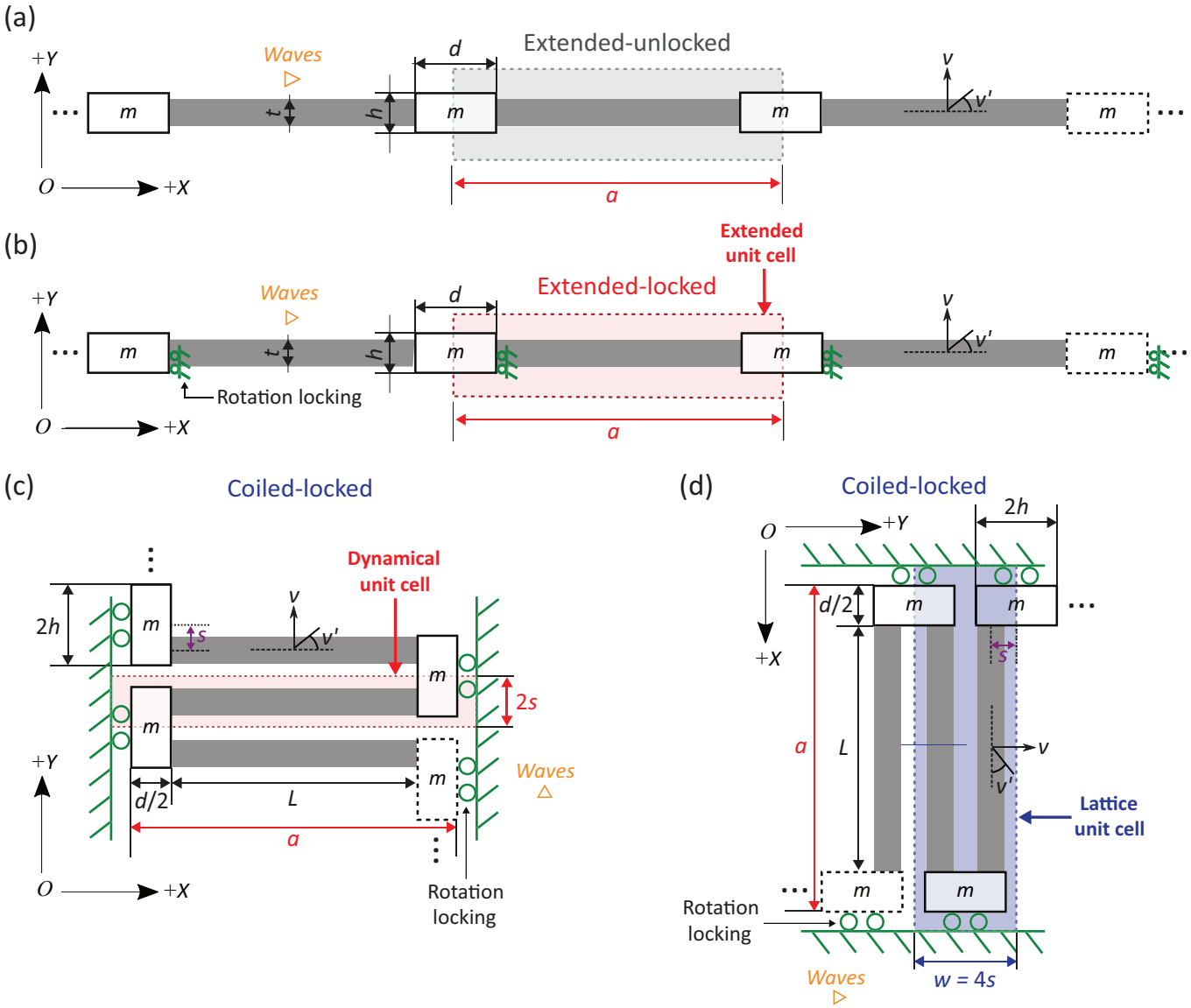

Figure 7. (Color online) Practical configuration of coiled PnC. (a) Extended-unlocked, (b) extended-locked, and (c) and (d) coiled-locked PnC are built up by tessellation of unit cells. In each case, all relevant dimensions are labeled, and in the case of the coiled-locked PnC, a distinction is drawn between (c) the "dynamical" unit cell, and (d) the repeated actual unit cell.

ysis, i.e., only the mass and stiffness submatrices of the frame elements governing bending wave motion are considered, and longitudinal rod displacements are disregarded. An experimental validation will then follow, in Section IV, on a very similar coiled PnC configuration that uses a symmetric design to enable practical realization of the periodic rotational locking.

Figure 7 shows representations of the (a) extended-unlocked, (b) extended-locked, and (c) and (d) coiled-locked PnC structures with labeled dimensions. In both extended PnC configurations, the lattice constant is a which, as shown in the figure, is the length of the primitive cell for the extended configuration. As illustrated in Fig. 7, the transformation from the extended-locked to the coiled-locked configuration occurs by cutting the extended-locked unit cell vertically at the half-mass point on either side and imposing an offset $\mp s$ between the mass center and the neutral axis of the beam segment, resulting in the *dynamic unit cell* shown in the pink box in Fig. 7(c). Note, the dynamic unit cell is equivalent to the extended-locked unit cell, due to the rotation locking. The coiled-locked lattice is built by alternating the sign of the offset at either end of the unit cell that have offsets of opposite sign where the masses are bonded at the top/bottom surfaces, rather than the left/right surfaces as was done in the extended configurations. This impacts the shape of the masses (i.e., they become longer in the Y direction and thinner in the X direction); however this has no dynamical consequence since the masses are rigid and the rotational degree of freedom at their

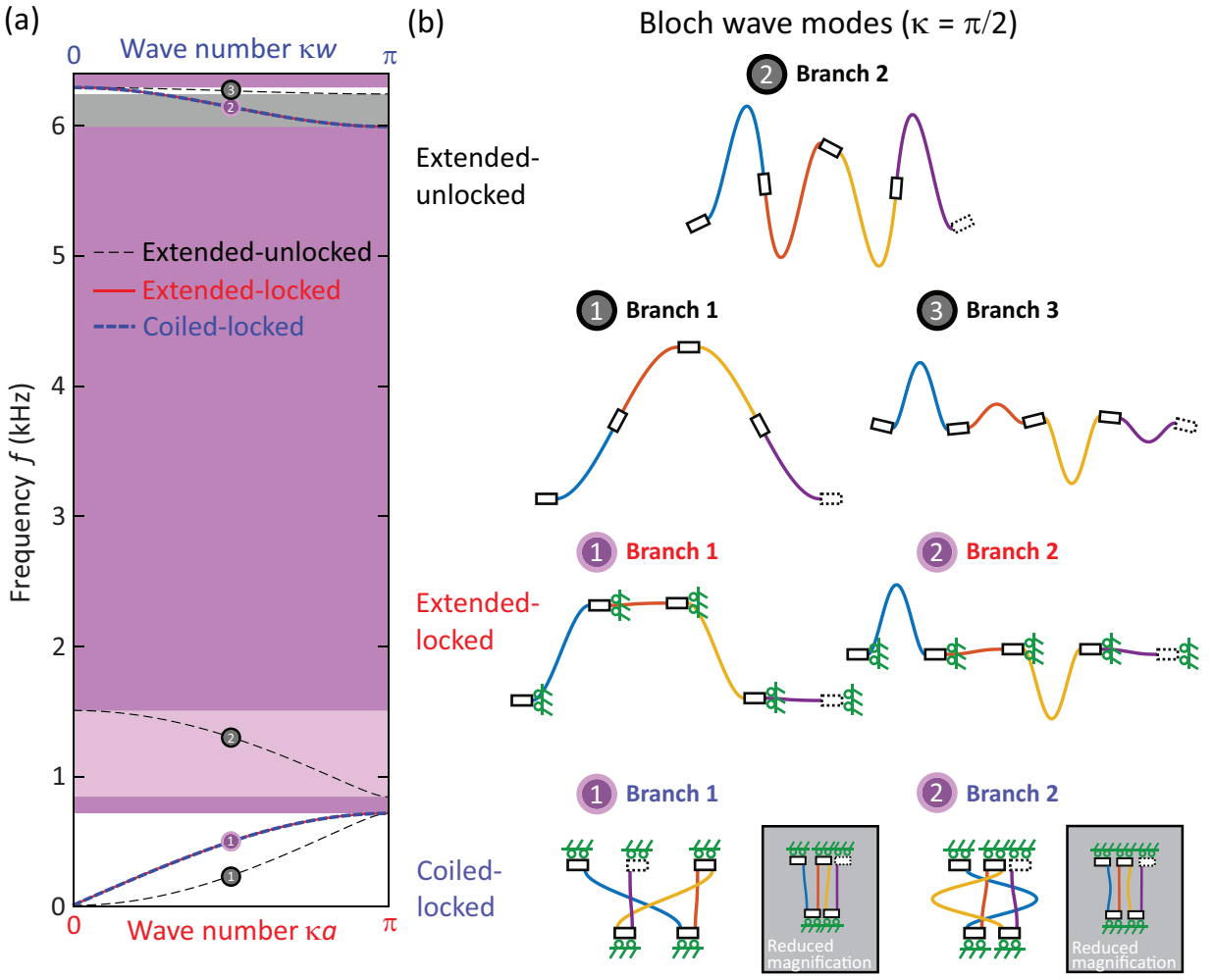

Figure 8. (Color online) (a) Dispersion curves of the extended-unlocked (thin black dashed), extended-locked (thick red), and coiled-locked (thick blue dashed) generated for the experimental parameters, give in Table II, and (b) associated Bloch mode shapes for each dispersion branch at wavenumber $\pi/2$. All modes shapes are magnified for ease of viewing. The coiled-locked mode shapes are also shown with reduced displacement magnification (in the light colored boxes) so that beam segments do not cross.

center is locked. Finally, the entire coiled-locked PnC is rotated by $-90°$ in Fig. 7(d), to align the Bloch wave directions of the extended-unlocked, extended-locked, and coiled-locked configurations, where the coiled *lattice unit cell* is shown in the blue box and has the reduced lattice constant w. The dynamic unit cell defines the minimum collection of system components that can properly represent the periodic motion of the unit cell, while the lattice unit cell is the one that is tessellated by repeated translations to form the total coiled PnC. Other permutations in the coiling of the PnC are possible. In this paper, the discussion is restricted to a single 2D case for simplicity, but the authors have previously conceived of a 3D coiled PnC in [56].

A comparison between the extended-unlocked (thin black dashed), extended-locked (thick red), and coiled-locked (thick blue dashed) dispersion curves using parameters of an experimental system, to be discussed in Sec. IV, are presented in Fig. 8(a), which includes the first three branches of the extended-unlocked PnC and the first two branches of both locked PnC configurations. The dispersion curves for the unlocked and locked cases are labeled with increasing indices in order of ascending pass-band frequency range and differentiated by either gray or purple circular markers, respectively. The band gaps of the extended-unlocked PnC are indicated by a gray shaded area, while the locked PnC band gaps are indicated by a light transparent magenta shading. Notice that the frequency axis is presented on a kHz scale, and thus the extended-locked and coiled-locked dispersion curves are identical (coiled-locked lies over extended-locked). The regions that are dark magenta correspond to shared band gap ranges, and the dark color is a result of the extended-unlocked gray band gap showing through the transparent magenta of the PnCs with rotation locking.

To visualize the differences between the spatial wave propagation behavior associated with each dispersion branch in Fig. 8(a), the Bloch mode shapes corresponding to a wavenumber of $\kappa a = \kappa w = \pi/2$ are plotted in Fig. 8(b). In each case, the unit cell mode shape is calculated, and then extended to three additional unit cell segments by the angular spectrum method [57, p. 90] in order to show a full Bloch wave period. The extended-unlocked Bloch modes graphically illustrate the rotation of the masses; where, in contrast, both the extended-locked and coiled-locked show no rotational displacement of the masses as dictated by the locking constraint.

IV. EXPERIMENTAL VALIDATION

An experimental embodiment of the coiled-locked PnC is realized in this section. Flexible aluminum beam segments are linked together by aluminum beam masses which are geometrically more stiff, to form the coiled PnC. Figure 9 shows a conceptual schematic of a symmetric back-to-back coiled PnC. By forming a symmetric structure, a symmetry axis (dashed orange) is imposed. It is known from elementary kinematics that when forces are applied along a symmetry axis, an equivalent half-model (blue boxed area) may be analyzed with rotations locked along the boundary created by the axis of symmetry. [52, pp. 256-260]. The presence of rigid-like masses (by appropriate choice of their material) in this symmetric setup enforces, to some approximation, the periodic rotational locking constraint imposed in the theoretical model. Since a half model is analyzed, the symmetric PnC must have two times the amount of mass at the masses lying on the symmetry axis to ensure proper periodicity of the unit cell in the analyzed half model. Additionally, only half the force is applied to the half model to ensure the correct response amplitude is obtained. The experimental symmetric coiled-locked PnC is shown in Fig. 9(b).

Parameter	Value	Unit
Bar thickness, t	1	mm
Bar width, b	5.08	mm
Bar length, L	29.5	mm
Mass height, h	17.79	mm
Mass width, d	17.4	mm
Unit-cell length (X-dir.), a	46.9	mm
Unit-cell length (Y-dir.), $w = 4s$	40.15	mm
Offset, s	10.04	mm
Coiling factor, $\beta = a/w$	1.17	
Young's modulus, E	68.9	GPa
Density, ρ	2700	kg/m^3
Periodic mass, m	2.58	g
Adapter mass, m_a	3.17	g
Loss factor, η	0 or 4×10^{-3}	

Table II. Properties of practical coiled PnC studied in Fig. 7, Fig. 8, and Fig. 9. Euler-Bernoulli beam theory can be safely applied for these parameters since the slenderness ratio is $\sigma_r = 29.5$, which is within the limits of the theory [55]. Note, dispersion curve calculations do not include damping, but the frequency response function in Fig. 9 (c) uses $\eta = 4 \times 10^{-3}$.

The symmetric coiled-locked PnC is characterized using a 4809-type vibration exciter, and a 8001-type impedance head by BKSV$^{\mathrm{TM}}$ to acquire the acceleration and force at the input point, which are used to generate a single-point accelerance frequency response function, i.e., $a_{\mathrm{inp}}/f_{\mathrm{inp}}$, where $a = \ddot{v}$. An equivalent FE model is used to generate the same accelerance curve over the frequency interval from 0 to 6.4 kHz. This is done by solving the governing equations of motion the finite extended-locked version of the structure based on Euler-Bernoulli beam elements as done in the preceding dispersion analysis. A loss factor is included in this calculation by replacing E with a damped Young's modulus $E_{\mathrm{d}} = E + \mathrm{i}\eta E$, where $\eta = 4 \times 10^{-3}$, to provide damping that was calibrated experimentally. Results of the FE computation and experiment are plotted in Fig. 9(c), and extremely good agreement is observed. The first band gap is shown as a gray shaded area, and within it no resonances are observed. The symmetry of the experimental PnC had the intended effect of locking the rotational degree of freedom at the masses, and the coiled PnC concept is experimentally validated.

V. CONCLUSIONS

This work presents a formal and unequivocal solution to the long-standing problem of elastic coiling, accompanied by a rigorous band-structure analysis demonstrating a complete and perfect conservation of normalized band structure with coiling. The concept is based on beam PnCs and comprises two simple, yet fundamental, mechanical transformations, namely, (1) a prescription of periodic rotational locking in the displacement field, and (2) full structural coiling at the locked locations. Rigid masses are added to the locked locations to facilitate experimental realization. A symmetric version of the configuration is implemented in the experiment to further enforce the periodic rotational locking constraint. The final outcome is a coiled PnC that represents an unprecedented physical mechanism in phononics, where a simple kinematic constraint is shown to enable perfect elastic coiling and realization of wide, subwavelength Bragg band gaps.

Since the discovery of phononic crystals (in the 1970's as periodic structures and early 1990's as phononic crystals) and locally resonant elastic metamaterials (in 2000), a key limitation has been the inability to simultaneously realize both wide and subwavelength band gaps. The coiled PnC concept proposed in the current investigation has overcome these fundamental limitations.

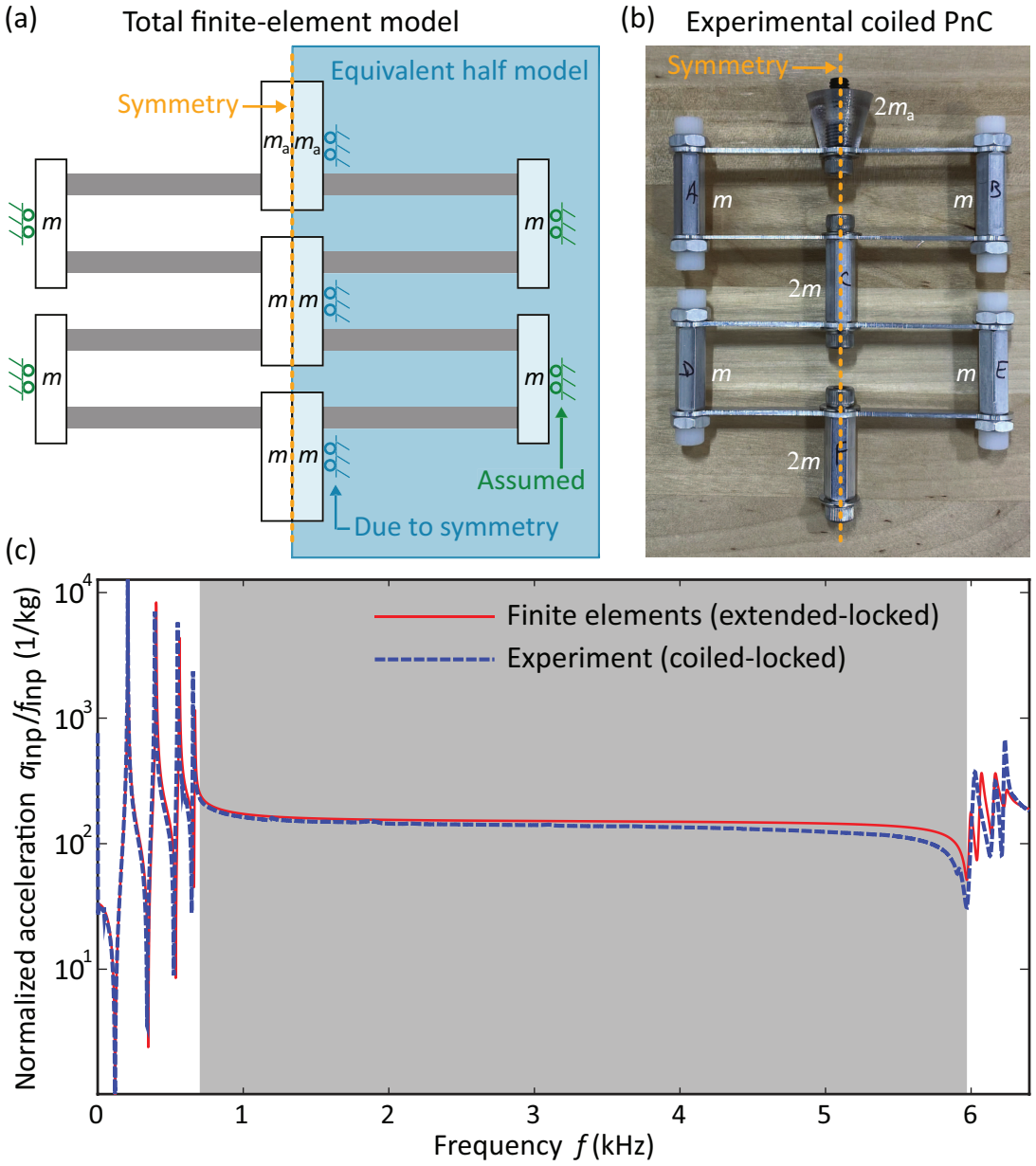

Figure 9. (Color online) Comparison of FE extended-locked PnC structure and the experimental coiled-locked structure. Coiled bar-mass model shown in (a), which is equivalent to the extended-locked PnC, is realized by manufacturing a PnC structure that uses the indicated symmetry plane to impose the roller conditions (i.e., no rotation) as shown (b). (c) Plots of single point accelerance at the input for the experimental measurement (dashed blue) and the FEM computation (solid red), with the first band-gap frequency range shaded in gray. An adapter mass is employed weighing in total m_a; this is a VeroClear 3D printed piece that sits between the experimental coiled PnC structure and the impedance head used for the measurement.

ACKNOWLEDGMENTS

This research is funded by the Air Force Office of Scientific Research under grant number 20RXCOR058.

DATA AVAILABILITY

All numerical data are generated directly using the equations presented. The experimental data are available upon reasonable request.

Appendix A: Stiffness and mass matrices of frame elements

Using an appropriate choice of FE shape functions, the elemental stiffness matrix of a frame element is written as

$$\mathbf{k}_f = \begin{bmatrix} \frac{AE}{2\alpha} & 0 & 0 & -\frac{AE}{2\alpha} & 0 & 0 \\ & \frac{3EI}{2\alpha^3} & \frac{3EI}{2\alpha^2} & 0 & -\frac{3EI}{2\alpha^3} & \frac{3EI}{2\alpha^2} \\ & & \frac{2EI}{\alpha} & 0 & -\frac{3EI}{2\alpha^2} & \frac{EI}{\alpha} \\ & & & \frac{AE}{2\alpha} & 0 & 0 \\ & sym. & & & \frac{3EI}{2\alpha^3} & -\frac{3EI}{2\alpha^2} \\ & & & & & \frac{2EI}{\alpha} \end{bmatrix}, \quad \text{(A1)}$$

where α is the half-length of the frame element, and *sym.* denotes that the matrix is symmetric.

The consistent mass matrix for the same element, formed using the same shape functions utilized for the stiffness matrix, is written as

$$\mathbf{m}_f = \frac{\rho A\alpha}{105} \begin{bmatrix} 70 & 0 & 0 & 35 & 0 & 0 \\ & 78 & 22\alpha & 0 & 27 & -13\alpha \\ & & 8\alpha^2 & 0 & 13\alpha & -6\alpha^2 \\ & & & 70 & 0 & 0 \\ & sym. & & & 78 & -22\alpha \\ & & & & & 8\alpha^2 \end{bmatrix}. \quad \text{(A2)}$$

Appendix B: Mass matrix for rigid mass

Rigid elements with distributed mass are represented using a mass matrix written as

$$\mathbf{m}_m = \begin{bmatrix} m & 0 & 0 \\ & m & 0 \\ sym. & & I_m \end{bmatrix}, \quad \text{(B1)}$$

where m is the rigid mass value, and I_m is the mass moment of inertia. In this work, all rigid masses are assumed to be cuboids, and thus

$$I_m = m(h^2 + d^2)/12, \quad \text{(B2)}$$

where h and d are the height and width of the rigid mass, respectively.

[1] D. Mead, A general theory of harmonic wave propagation in linear periodic systems with multiple coupling, J. Sound Vib. **27**, 235 (1973).
[2] M. M. Sigalas and E. N. Economou, Elastic and acoustic wave band structure, J. Sound Vib. **158**, 377 (1992).
[3] M. S. Kushwaha, P. Halevi, L. Dobrzynski, and B. Djafari-Rouhani, Acoustic band structure of periodic elastic composites, Phys. Rev. Lett. **71**, 2022 (1993).
[4] M. I. Hussein, G. M. Hulbert, and R. A. Scott, Dispersive elastodynamics of 1D banded materials and structures: analysis, J. Sound Vib. (UK) **289**, 779 (2006).
[5] P. A. Deymier, ed., *Acoustic Metamaterials and Phononic Crystals*, Springer Series in Solid-State Sciences (Springer, Berlin, 2013).
[6] V. Laude, *Phononic Crystals: Artificial Crystals for Sonic, Acoustic, and Elastic Waves* (de Gruyter Co, Berlin, 2015).
[7] A. Khelif and A. Adibi, *Phononic Crystals: Fundamentals and Applications* (Springer, Berlin, 2015).
[8] A. S. Phani and M. I. Hussein, eds., *Dynamics of Lattice Materials* (John Wiley & Sons, New Jersey, 2017).
[9] M. Maldovan, Sound and heat revolutions in phononics, Nature **503**, 209 (2013).
[10] M. I. Hussein, M. J. Leamy, and M. Ruzzene, Dynamics of phononic materials and structures: Historical origins, recent progress, and future outlook, Appl. Mech. Rev. **66** (2014).
[11] Z. Liu, X. Zhang, Y. Mao, Y. Y. Zhu, Z. Yang, C. T. Chan, and P. Sheng, Locally Resonant Sonic Materials, Science **289**, 1734 (2000).
[12] P. F. Pai and G. Huang, eds., *Theory and Design of Acoustic Metamaterials* (SPIE Press, Bellingham, Washington, 2015).
[13] P. Sheng, X. X. Zhang, Z. Liu, and C. T. Chan, Locally resonant sonic materials, Physica B **338**, 201 (2003).
[14] Y. Xiao, J. Wen, and X. Wen, Broadband locally resonant beams containing multiple periodic arrays of attached resonators, Phys. Lett. A **376**, 1384 (2012).
[15] N. M. M. Frandsen, O. R. Bilal, J. S. Jensen, and M. I. Hussein, Inertial amplification of continuous structures: Large band gaps from small masses, J. Appl. Phys. **119**, 124902 (2016).
[16] K. H. Matlack, A. Bauhofer, S. Krödel, A. Palermo, and C. Daraio, Composite 3D-printed metastructures for low-frequency and broadband vibration absorption, P. Natl. Acad. Sci. USA **113**, 8386 (2016), https://www.pnas.org/content/113/30/8386.full.pdf.

[17] K. H. Matlack, M. Serra-Garcia, A. Palermo, S. D. Huber, and C. Daraio, Designing perturbative metamaterials from discrete models, Nat. Mater. **17**, 323 (2018).

[18] J. Meaud and K. Che, Tuning elastic wave propagation in multistable architected materials, Int. J. Solids Struct. **122-123**, 69 (2017).

[19] O. Thorp, M. Ruzzene, and A. Baz, Attenuation and localization of wave propagation in rods with periodic shunted piezoelectric patches, Proc. SPIE **4331**, 218 (2001).

[20] F. Casadei, T. Delpero, A. Bergamini, P. Ermanni, and M. Ruzzene, Piezoelectric resonator arrays for tunable acoustic waveguides and metamaterials, J. Appl. Phys. **112**, 064902 (5 pp.) (2012).

[21] C. D. Pierce, C. L. Willey, V. W. Chen, J. O. Hardin, J. D. Berrigan, A. T. Juhl, and K. H. Matlack, Adaptive elastic metastructures from magneto-active elastomers, Smart Mater. Struct. **29**, 065004 (2020).

[22] J. Callanan, C. Willey, V. Chen, J. Liu, M. Nouh, and A. Juhl, Uncovering low frequency band gaps in electrically resonant metamaterials through tuned dissipation and negative impedance conversion, Smart Mater. Struct **31**, 015002 (2021).

[23] C. Yilmaz, G. M. Hulbert, and N. Kikuchi, Phononic band gaps induced by inertial amplification in periodic media, Phys. Rev. B **76**, 54309 (2007).

[24] G. Acar and C. Yilmaz, Experimental and numerical evidence for the existence of wide and deep phononic gaps induced by inertial amplification in two-dimensional solid structures, J. Sound Vib. **332**, 6389 (2013).

[25] Z. Liang and J. Li, Extreme acoustic metamaterial by coiling up space, Phys. Rev. Lett. **108**, 114301 (2012).

[26] J. Christensen, L. Martin-Moreno, and F. J. Garcia-Vidal, Theory of resonant acoustic transmission through subwavelength apertures, Phys. Rev. Lett. **101**, 014301 (2008).

[27] Y. Li and B. M. Assouar, Acoustic metasurface-based perfect absorber with deep subwavelength thickness, Appl. Phys. Lett. **108**, 063502 (2016).

[28] Y. Xie, B.-I. Popa, L. Zigoneanu, and S. A. Cummer, Measurement of a broadband negative index with space-coiling acoustic metamaterials, Phys. Rev. Lett. **110**, 175501 (2013).

[29] Y. Li, B. Liang, X.-Y. Zou, and J.-C. Cheng, Extraordinary acoustic transmission through ultrathin acoustic metamaterials by coiling up space, Appl. Phys. Lett. **103**, 063509 (2013).

[30] B. Yuan, Y. Cheng, and X. Liu, Conversion of sound radiation pattern via gradient acoustic metasurface with space-coiling structure, Appl. Phys. Express **8**, 027301 (2015).

[31] M. Molerón, M. Serra-Garcia, and C. Daraio, Visco-thermal effects in acoustic metamaterials: from total transmission to total reflection and high absorption, New J. Phys. **18** (2016).

[32] A. O. Krushynska, F. Bosia, and N. M. Pugno, Labyrinthine acoustic metamaterials with space-coiling channels for low-frequency sound control, Acta Acust. United Ac. **104**, 200 (2018).

[33] Y. Li, B. Liang, X. Tao, X.-f. Zhu, X.-Y. Zou, and J.-C. Cheng, Acoustic focusing by coiling up space, Appl. Phys. Lett. **101**, 233508 (2012).

[34] S. Zuo, Q. Wei, Y. Tian, Y. Cheng, and X. Liu, Acoustic analog computing system based on labyrinthine metasurfaces, Sci. Rep. **8**, 10103 (2018).

[35] T. Chen, J. Jiao, and D. Yu, Enhanced broadband acoustic sensing in gradient coiled metamaterials, J. Phys. D Appl. Phys. **54**, 085501 (2020).

[36] B. Assouar, S. Qi, and Y. Li, Acoustic metamaterials and metasurfaces: a transformative approach for phononic insulators and energy harvesting, in *Quantum Sensing and Nano Electronics and Photonics XIV*, Vol. 10111, edited by M. Razeghi, International Society for Optics and Photonics (SPIE, 2017) pp. 340 – 348.

[37] Y. Wang, H. Zhao, H. Yang, J. Zhong, and J. Wen, A space-coiled acoustic metamaterial with tunable low-frequency sound absorption, Europhys. Lett. **120**, 54001 (2017).

[38] Y. Wang, H. Zhao, H. Yang, J. Zhong, D. Zhao, Z. Lu, and J. Wen, A tunable sound-absorbing metamaterial based on coiled-up space, J. Appl. Phys. **123**, 185109 (2018).

[39] G. Y. Song, B. Huang, H. Y. Dong, Q. Cheng, and T. J. Cui, Broadband focusing acoustic lens based on fractal metamaterials, Sci. Rep. **6**, 35929 (2016).

[40] G. Y. Song, Q. Cheng, B. Huang, H. Y. Dong, and T. J. Cui, Broadband fractal acoustic metamaterials for low-frequency sound attenuation, Appl. Phys. Lett. **109**, 131901 (2016).

[41] H. T. Sun, J. S. Wang, Y. Cheng, Q. Wei, and X. J. Liu, Modulation of water surface waves with a coiling-up-space metasurface, AIP Adv. **6**, 055017 (2016).

[42] J. Liu, L. Li, B. Xia, and X. Man, Fractal labyrinthine acoustic metamaterial in planar lattices, Int. J. Solids Struct. **132-133**, 20 (2018).

[43] M. Ruzzene and F. Scarpa, Directional and band-gap behavior of periodic auxetic lattices, Phys. Status Solidi b **242**, 665 (2005).

[44] A. S. Phani, J. Woodhouse, and N. A. Fleck, Wave propagation in two-dimensional periodic lattices, J. Acoust. Soc. Am. **119**, 1995 (2006).

[45] R. Langley, N. Bardell, and H. Ruivo, The response of two-dimensional periodic structures to harmonic point loading a theoretical and experimental study of a beam grillage, J. Sound Vib. **207**, 410 (1997).

[46] Y.-F. Wang, Y.-S. Wang, and C. Zhang, Bandgaps and directional propagation of elastic waves in 2d square zigzag lattice structures, J. Phys. D: Appl. Phys **47**, 485102 (2014).

[47] Y. Liu, Z. Liang, F. Liu, O. Diba, A. Lamb, and J. Li, Source illusion devices for flexural lamb waves using elastic metasurfaces, Phys. Rev. Lett. **119**, 034301 (2017).

[48] G. J. Jeon and J. H. Oh, Elastic coiling-up-space metamaterial, Phys. Rev. Appl. **16**, 064016 (2021).

[49] M. I. Hussein, S. Biringen, O. R. Bilal, and A. Kucala, Flow stabilization by subsurface phonons, Roc. R. Soc. A **471**, 20140928 (2015).
[50] Euler-Bernoulli beam theory is applicable to slender beams, which is the case for all models considered in this paper. For thicker beams, Timoshenko beam theory may be used [58].
[51] T. J. R. Hughes, *The finite element method* (Prentice-Hall, New Jersey, 1987).
[52] G. R. Liu and S. S. Quek, *The Finite Element Method: A Practical Course* (Elsevier Science, Oxford, UK, 2003).
[53] F. Bloch, Über die quantenmechanik der elektronen in kristallgittern, Z. Phys. **52**, 555 (1929).
[54] M. Ruzzene, F. Scarpa, and F. Soranna, Wave beaming effects in two-dimensional cellular structures, Smart Mat. Struct. **12**, 363 (2003).
[55] E. Oñate, Thick/slender plane beams. Timoshenko theory, in *Structural Analysis with the Finite Element Method Linear Statics: Volun* (Springer Netherlands, Dordrecht, NL, 2013) pp. 37–97.
[56] C. J. Barnes, C. L. Willey, K. Rosenberg, A. Medina, and A. T. Juhl, Initial computational investigation toward passive transition delay using a phononic subsurface, in *AIAA Scitech 2021 Forum* (Virtual, 2021) pp. 1 – 23.
[57] E. G. Williams, *Fourier Acoustics: Sound Radiation and Nearfield Acoustic Holography* (Academic Press, London, 1999).
[58] L. Liu and M. I. Hussein, Wave motion in periodic flexural beams and characterization of the transition between Bragg scattering and local resonance, J. Appl. Mech. **79**, 011003 (2012).